Journal of Medical Imaging

MedicalImaging.SPIEDigitalLibrary.org

Coherent scatter imaging Monte Carlo simulation

Laila Hassan
Carolyn A. MacDonald

SPIE.

Laila Hassan, Carolyn A. MacDonald, "Coherent scatter imaging Monte Carlo simulation," *J. Med. Imag.* **3**(3), 033504 (2016), doi: 10.1117/1.JMI.3.3.033504.

Coherent scatter imaging Monte Carlo simulation

Laila Hassan and Carolyn A. MacDonald*
University at Albany, State University of New York, Department of Physics, 1400 Washington Avenue, Albany, New York 12222, United States

Abstract. Conventional mammography can suffer from poor contrast between healthy and cancerous tissues due to the small difference in attenuation properties. Coherent scatter slot scan imaging is an imaging technique which provides additional information and is compatible with conventional mammography. A Monte Carlo simulation of coherent scatter slot scan imaging was performed to assess its performance and provide system optimization. Coherent scatter could be exploited using a system similar to conventional slot scan mammography system with antiscatter grids tilted at the characteristic angle of cancerous tissues. System optimization was performed across several parameters, including source voltage, tilt angle, grid distances, grid ratio, and shielding geometry. The simulated carcinomas were detectable for tumors as small as 5 mm in diameter, so coherent scatter analysis using a wide-slot setup could be promising as an enhancement for screening mammography. Employing coherent scatter information simultaneously with conventional mammography could yield a conventional high spatial resolution image with additional coherent scatter information. [DOI: 10.1117/1.JMI.3.3.033504]

Keywords: coherent scattering; breast cancer; Monte Carlo simulation.

Paper 15208RR received Oct. 20, 2015; accepted for publication Aug. 1, 2016; published online Aug. 26, 2016.

1 Introduction

Conventional mammography can suffer from both false positives and false negatives.[1] Abnormalities at early stages with less than palpable size can be missed. Coherent scattering imaging is an innovative imaging technique which exploits the scatter normally eliminated in conventional mammography. Coherent scatter imaging is sensitive to disease at very early stages compared to conventional imaging.[2] Diffraction, which is the constructive interference of coherent scattered radiation, is highly dependent on a material's molecular structure.[3] Coherent scatter signals for tissues typically have been studied using a conventional diffraction measurement geometry. Evans et al.[4] measured the angular distribution of scattered photons from diseased and normal breast tissue samples. They showed that adipose tissue could be clearly distinguished from carcinoma. Kidane et al.[5] measured the scattering profiles of excised breast tissue samples. There was a change in maximum intensity of x-ray diffraction profiles at 1.1 nm^{-1} by a factor of 2 between adipose and fat-free tissues. Griffiths et al.[6] performed diffraction micro-CT measurements on breast tissue samples. They concluded that identification of different breast tissues is promising, finding a clear correlation between diffraction images and stained histopathological sections. Harris et al.[7] demonstrated that a contrast enhancement of 60% to 100% was achieved in the diffraction relative to conventional images. All of these studies required a small beam diameter. This technique is not compatible with screening mammography since it would require two-dimensional raster scanning. In addition to the experimental work, many studies have used Monte Carlo simulations to investigate this technique further. Taibi et al.[8] used form factor data from x-ray diffraction measurements in the EGS4 Monte Carlo code to model a breast imaging system that makes use of a scatter signal. Simulation results confirmed that the contrast between healthy and tumor tissue is greater than that of the primary image. Kapadia et al.[9] used a coded-aperture x-ray scatter imaging system and a GEANT4 simulation to study coherent scatter diffraction patterns. Similar results were found by Elshemey et al.[10] Lakshmanan et al. [11,12] described a tumor margin evaluation method based on x-ray coherent scatter computed tomography imaging using a Monte Carlo Geant4 code. The resulting images distinguish cancerous tumors embedded in complex distributions of adipose and fibroglandular tissue.

In this study, an imaging technique[13–15] compatible with screening mammography was investigated using a Monte Carlo simulation. The coherent scatter technique employed a wide-slot system such as the one used in slot scan mammography. The coherent scatter was collected by placing two grid/detector strips alongside the usual grid/strip used for the transmission image, as shown in Fig. 1. These two grids were tilted to the desired scattering angle to preferentially transmit the coherent scatter signal across a wide-field imaging for rapid imaging. Unlike the previous studies of coherent scatter properties, the goal here is simply to highlight the tissue which scatters at a particular angle to emphasize this area on the conventional mammogram, which would be collected simultaneously.

This system does not require any additional radiation and, unlike computed tomography, does not require multiple exposures. Once optimized, the coherent scatter information could be overlaid on the simultaneously collected conventional mammogram. Thus, the coherent scatter image does not require high resolution.[16] Since the new information is collected simultaneously with a conventional mammogram, the goal of this study is not to compare the two techniques, but to assess whether regions of different tissue types could be visible in the coherent scatter image collected under compatible conditions.

The simulation was designed to rapidly assess the optimization of the system parameters such as tilt angles, grid ratios, and

*Address all correspondence to: Carolyn A. MacDonald, E-mail: cmacdonald@albany.edu

2329-4302/2016/$25.00

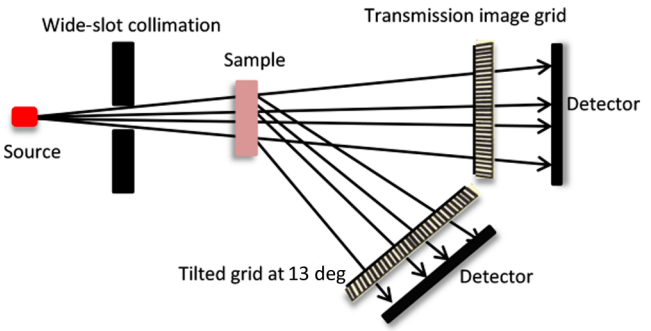

Fig. 1 A wide-slot system (top view) is used to collect coherent scatter signal along with transmission signal. The additional grid is tilted with respect to the primary beam to preferentially pass the carcinoma signal. A third grid could be added on the other side of the direct beam (toward the top of the figure) to collect additional signal. The slot width was set to 5 mm.

shields. Results show that coherent scatter analysis using a wide-slot setup might be promising as an enhancement for screening mammography. The addition of tissue-specific information may have the potential to improve screening mammography.

2 Wide-Slot Coherent Scattering Imaging

Scatter normally degrades the transmission image contrast; thus it is typically removed in conventional mammography using antiscatter grids. When scattered photons hit the grid, the grid preferentially absorbs them and transmits the primary photons. In the system shown in Fig. 1, a system similar to a wide-slot mammography system has been modified to collect the coherent scatter signal.[16] Conventional scanning system slot widths range from 4 to 14 mm.[17] For the simulation here, the width of the slot was set to 5 mm. In addition to the usual antiscatter grid, a second grid is tilted at the characteristic angle for scatter from a specific tissue type, e.g., carcinoma, to preferentially pass the carcinoma signal and block the scatter from healthy breast tissue. For example, the grid could be titled at 13 deg, which corresponds to the scattering angle of carcinoma at the Kα line (17.4 keV)[18] for a molybdenum anode source. Alternatively, two selection grids could be used, collecting simultaneously from different angles, to provide simultaneous images of the presence of different tissue types, as well as the conventional transmission image. Additional grids could be placed on the other side of the direct beam (toward the top of Fig. 1) to double the signal and provide depth information.

This technique would produce a wide-field image rapidly enough for real-time collection. Coherent scatter would be collected from the entire area of the wide-slot system with the potential to give a spatially resolved tissue-specific signal[16] compatible with screening mammography.

3 Monte Carlo Simulations

The simulation in this study is a simple single purpose Monte Carlo MATLAB® code. It models photon interactions and propagation using the knowledge of probability distributions for individual interactions. The modeled phantoms are cancer, fat, and normal breast tissue (50% fat, 50% fibroglandular tissue). The purpose of the simulation is to enable prediction of the results for real tissues and to optimize geometry. Since the angular selectivity in the modeled imaging system is of low resolution, the code in this study used a simple Gaussian to model the coherent scatter peaks using literature values of peak position and peak width. It is designed solely to model this imaging system. It also differs from standard modeling programs, such as SHADOW[19] and MCNP,[20] in that those codes are not designed to handle interference effects within the samples.

3.1 *Algorithm*

A simple model was developed to approximate the experimental system of Fig. 1 and to provide some information about parameter optimization. The sequence of simulated events is shown in Fig. 2. First a vector is calculated from a random point on the source, which has a circular cross section, to a random point within the sample slot. The sample is modeled as a three-dimensional matrix and each voxel is assigned a material. When a random point (x, y, and z) is selected inside the sample, the code identifies which material it hits and performs a suitable interaction depending on the material properties, such as coherent scatter cross section, absorption cross section, and Compton scatter cross section. The photon is then propagated to the next slice. If a photon is absorbed, it is eliminated. If it is Compton scattered, it deviates from the original path with a random angle, θ, and a random azimuthal angle, φ. If it is diffracted, it is scattered near the characteristic scattering angle. Photons passing out of sample are propagated toward the detector past grids, shields, or combinations of both. Finally, the transmitted photons hit the detector.

3.1.1 *Interaction probability calculations*

The probability for a photon–tissue interaction was calculated using Beer–Lambert's law[21]

$$\frac{I}{I_o} = e^{-\mu t}, \tag{1}$$

where I_o is the incident beam, I is the transmitted beam, t is the material thickness, and μ is the total linear attenuation coefficient

$$\mu = \mu_{\text{abs}} + \mu_{\text{C}} + \mu_{\text{diff}}, \tag{2}$$

where μ_{abs}, μ_{C}, and μ_{diff} are the absorption, Compton, and coherent scatter linear coefficients, respectively. Beer–Lambert's law arises from the differential equations for the amount of beam lost in a very thin slice of width dx. To assess the net intensity of the diffracted beam alone, it is necessary to consider all three effects. If the incident beam intensity is I_o, and the resultant transmitted beam intensity is I, there is also a diffracted beam of intensity I_{diff}, a Compton scattered beam of intensity I_{C}, and absorption amount I_{abs}. The change in the intensity of the diffracted beam I_{diff}, in passing through a thickness dx of material was assumed to be

$$\text{d}I_{\text{diff}} = -I_{\text{diff}}(\mu_{\text{abs}} + \mu_{\text{C}})\text{d}x + I\mu_{\text{diff}}\text{d}x, \tag{3}$$

where the negative first term is the loss from absorption and scatter and the second term is the growth of the diffracted beam due to diffraction from the primary beam.

Similarly, the change in the intensity of the Compton scattered beam I_{C} was assumed to be

$$\text{d}I_{\text{C}} = -I_{\text{C}}(\mu_{\text{abs}})\text{d}x + (I + I_{\text{diff}})\mu_{\text{C}}\text{d}x. \tag{4}$$

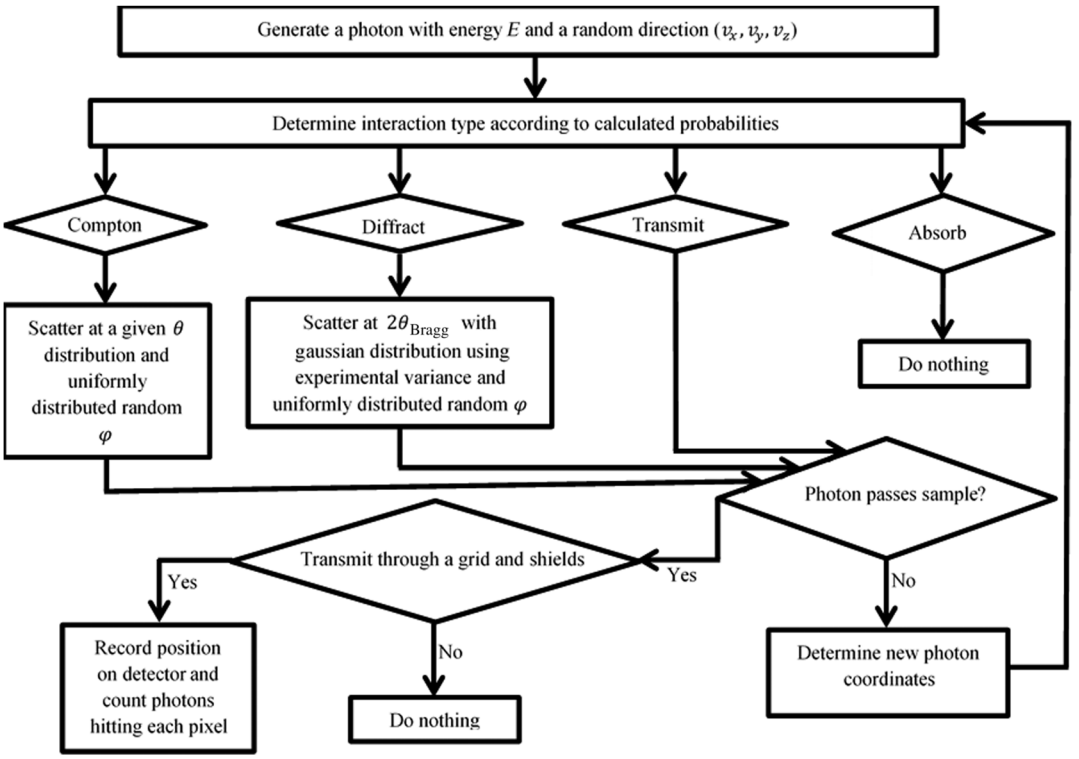

Fig. 2 Block diagram illustrating the main steps of the simulation algorithm.

Note that photons which diffract and then Compton scatter or Compton scatter and then diffract, in either order, are counted to be scattered, as they will not fall within the diffraction cone.

The increase in the absorbed intensity, I_{abs}, is

$$\mathrm{d}I_{\text{abs}} = (I + I_{\text{C}} + I_d)\mu_{\text{abs}}\mathrm{d}x. \tag{5}$$

Here again any combination of scatter plus absorption counts as absorption. The probability of absorption, p_{abs}, Compton scattering, p_{C}, diffraction, p_{diff}, and transmission, p_T, in a layer of thickness t was thus calculated from the differential equations as

$$p_{\text{abs}} = 1 - e^{-\mu_{\text{abs}}t}, \tag{6}$$

$$p_{\text{C}} = (1 - e^{-\mu_C t})e^{-\mu_{\text{abs}}t}, \tag{7}$$

$$p_{\text{diff}} = (1 - e^{-\mu_{\text{diff}}t})e^{-(\mu_{\text{abs}}+\mu_C)t}, \tag{8}$$

and

$$p_T = 1 - (p_{\text{abs}} + p_C + p_{\text{diff}}). \tag{9}$$

Cumulative distribution functions (CDF) for these four discrete probabilities were computed and organized in an array. Then, pseudorandom sampling was performed using a linear search method to simulate interaction probability distributions.

3.1.2 *Propagation through sample slices*

The sample was broken into slices along the beam direction to account for multiple interactions and to allow for complex geometries. The number of interactions should agree regardless of the number of slices. To test this, a homogenous phantom was broken into two slices and the resultant numbers of interactions were compared to that of the bulk phantom. The results are shown in Table 1. Simulation results for the number of photons for different interactions using a graphite sample in a single block are shown as one slice or divided into two slices. There is an agreement between the two, as expected, except that using two slices introduces double diffraction. The number of photons which are double diffracted reduces the number of photons in the diffraction ring and makes the total single diffraction number less for two slices than for a single slice. The uncertainty was assumed to be purely Poisson and was computed as

$$\sigma = \sqrt{N}, \tag{10}$$

where N is the number of photons.

3.2 *Interaction Cross Sections*

3.2.1 *Absorption*

Tables of photoabsorption coefficients were taken from the National Institute of Standards and Technology Database.[22]

Table 1 Simulation results for the number of photons for different interactions using a graphite sample in a single block, as one slice or divided into two slices.

Interaction	One slice	Two slices
#Absorbed	71831 ± 268	71704 ± 268
#Compton	11892 ± 109	12018 ± 110
#Transmitted	15097 ± 123	15130 ± 123
#Diffracted	1180 ± 34	1126 ± 34
#Double diffracted	0	22 ± 5

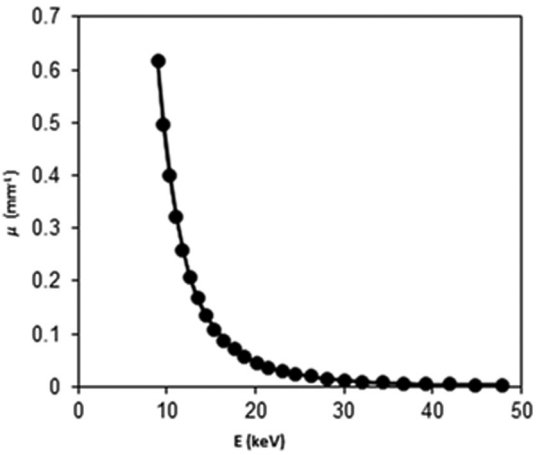

Fig. 3 Data (circles from Ref. 22) and fit (solid line) of absorption coefficients versus energy for carbon.

The photoabsorbtion coefficients were plotted against energy E and fitted to an inverse cubic for carbon, hydrogen, and oxygen, which are the main constituents of fat. Figure 3 shows the fitting results for carbon. The fitting results were taken as

$$\mu_{\text{carbon}} = \frac{4.25 \times 10^2 (\text{keV}^3\ \text{mm}^{-1})}{E^3}, \tag{11}$$

$$\mu_{\text{hydrogen}} = \frac{4.5 \times 10^{-5} (\text{keV}^3\ \text{mm}^{-1})}{E^3}, \tag{12}$$

and

$$\mu_{\text{oxygen}} = \frac{7.2 \times 10^{-1} (\text{keV}^3\ \text{mm}^{-1})}{E^3}. \tag{13}$$

The absorption coefficients for fat, fibroglandular tissue, and carcinoma were then determined using the weighted fraction of constituent elements[23] as

$$\mu = \rho \sum_i \frac{w_i \mu_i}{\rho_i}, \tag{14}$$

where ρ is the density and ρ_i and w_i are the density and the fraction by weight of the i'th element constituent. The densities of carbon, oxygen, and hydrogen are 1.7, 1.3×10^{-3} and 8.4×10^{-5} g/cm^3, respectively.[23] The densities of fat, fibroglandular tissue, and carcinoma are 0.95, 1.04, and 1.07 g/cm^3, respectively.[23,24] The weight fractions, w, for carbon, oxygen, and hydrogen in fat, were taken as 0.598, 0.278, and 0.114, respectively.[24] For carcinoma, the weight fractions for carbon, oxygen, and hydrogen were 0.194, 0.66, and 0.1, respectively.[25] For fibroglandular tissue, the weight fractions for carbon, oxygen, and hydrogen were 0.185, 0.68, and 0.094, respectively.[24]

3.2.2 *Compton scatter*

The Compton scattering coefficients were taken from the tables of the Center of X-ray Optics at Lawrence Berkeley National Laboratory's Materials Sciences Division.[26] Data were fitted to a polynomial. The Compton scattering coefficients μ_C in the energy range of 10 to 30 keV for carbon, hydrogen, and oxygen were plotted against energy E and fitted to polynomials.

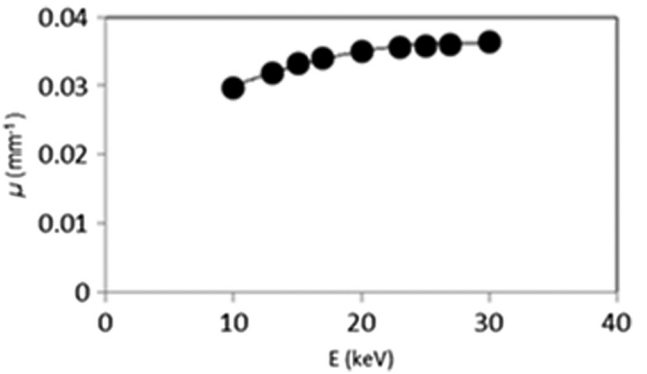

Fig. 4 Data (circles from Ref. 26) and fit (solid line) of Compton scatter coefficients versus energy for carbon.

Figure 4 shows the fitting results for carbon. The fitting functions for carbon, hydrogen, and oxygen were taken as

$$\mu_{\text{C\_Carbon}} = -2 \times 10^{-5} (\text{keV}^{-2}\ \text{mm}^{-1}) E^2 + 1.1 \times 10^{-3} (\text{keV}^{-1}\ \text{mm}^{-1}) E + 2.1 \times 10^{-2}\ (\text{mm}^{-1}), \tag{15}$$

$$\mu_{\text{C\_Hydrogen}} = 3.2 \times 10^{-6}\ (\text{mm}^{-1}), \tag{16}$$

$$\mu_{\text{C\_Oxygen}} = 2 \times 10^{-7} (\text{keV}^{-1}\ \text{mm}^{-1}) E + 2 \times 10^{-5}\ (\text{mm}^{-1}). \tag{17}$$

For these low energies, the probability of Compton scatter is nearly independent of energy.

The angular distribution of Compton scatter is crucial in the simulation process. It accounts for the background of the coherent scatter signal. Compton scatter is often considered to be approximately isotropic.[27] However, to accurately model the coherent scatter signal, the actual Compton scatter distribution was simulated, especially the drop in cross section at low angles. The differential Compton cross section for 17.44 keV photons versus scattering angle for fat is plotted in Fig. 5.[28] In the

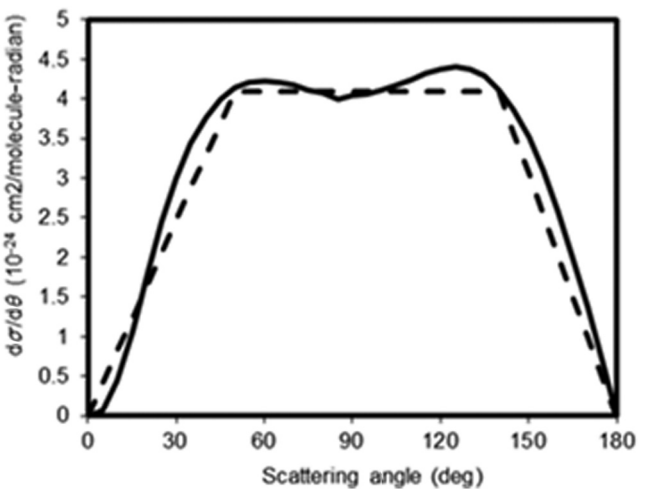

Fig. 5 Fat Compton scattering cross sections versus scattering angle at photon energy of 17.44 keV, data (solid line from data of Ref. 28) and a crude approximation (dashed line).

simulations, the emphasis is at the low angles, where the diffraction signal is located. For simplicity, a crude approximation was used in the code to increase computation efficiency. Since the scatter at angles larger than 50 deg will not hit the detector, the cross section was approximated as a constant cross section above that angle. This distribution was also used for cancer and fibroglandular tissue as an approximation.

3.2.3 *Coherent scatter*

The theoretical diffracted intensity I per unit length of a diffraction ring from the (hkl) plane of a crystal is[29]

$$I = I_o r_e^2 \frac{1+\cos^2\theta}{2} \frac{1}{2\sin^2\frac{\theta}{2}\cos\frac{\theta}{2}} \lambda^3 F_{hkl}^2 n \frac{1}{V_c^2} Dt, \tag{18}$$

where I_o is the intensity per unit area of the incident beam, r_e is the classical electron radius, θ is the scattering angle, λ is the wavelength of the incident X-ray, F_{hkl} is the structure factor for the (hkl) lattice plane, n is the multiplicity factor for the (hkl) planes, V_c is the volume of a unit cell of the crystal, D is the Debye factor, and t is the thickness of the sample. The diffraction probability was taken as

$$p_{\text{diff}} = \frac{I}{I_o}. \tag{19}$$

This is not applicable for an amorphous material such as tissue. However, early experimental measurements[13–15] had been performed with the imaging system using graphite, and those measurements included comparisons with fatty tissue. Equation (19) was used to compute the diffraction probability for graphite. The theoretical diffracted intensity for fat is not available since it involves calculations of the Fourier transform of the poorly known radial distribution function. Thus, the code used the theoretical value for graphite and simply multiplied it by the experimental ratio between fat and graphite diffracted integrated intensities to determine the diffraction probability from fat. This is equivalent to employing the experimental ratio of I/I_o for fat, but obviates the issue of image overexposure from the direct beam I_o.

The peak width for the two materials is also a crucial parameter for the simulation and was obtained from experimental work. Figure 6 shows the experimental setup used to determine the diffracted intensities for graphite and fat and their peak widths. Since the incident beam intensity can vary significantly with small changes in power supply voltage, the diffraction experiment was performed on fat and graphite simultaneously. The two materials were irradiated with two pencil beams

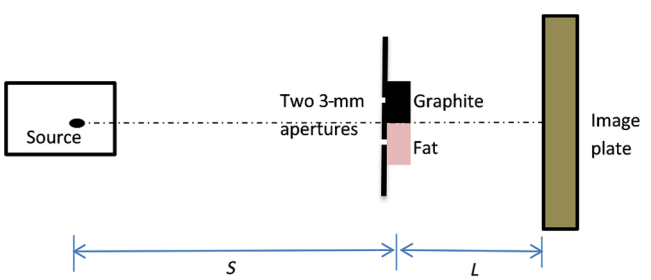

Fig. 6 Experimental setup for determining the diffracted intensity for fat and graphite. *S* is the source-to-sample distance and *L* is the sample-to-image plate distance. *S* is 445 mm and *L* is 75 mm.

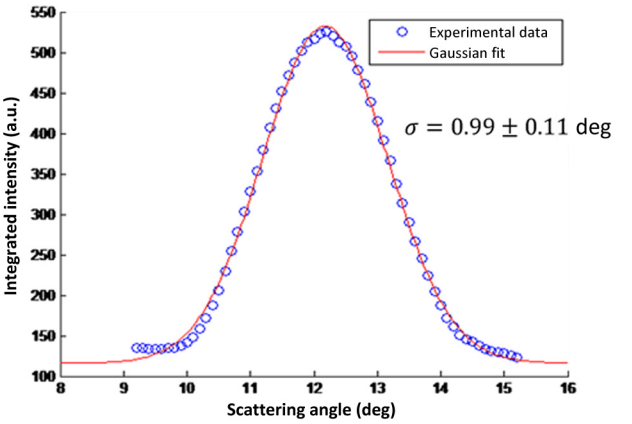

Fig. 7 The Gaussian fit of integrated intensity of the diffraction ring for graphite.

coming from one source, an Oxford apogee with an Mo anode. The source was run at 47.5 kV and 0.95 mA. A 138-μm Zr filter was used to reduce Mo Kβ line. Two 3-mm apertures were used in front of the sample to define the size of the incident x-ray beam. A Fuji image plate was used to record the two diffraction rings. The radially integrated intensity experimental profiles of the rings were calculated using Fit2D.[30] From these profiles, a Gaussian fit was used to determine the total integrated intensity and width for both peaks. In the simulation, the natural width of graphite was taken as zero degrees since the width for the graphite peak was shown to be mainly due to the sample geometry. The broadening due to the source divergence and the large irradiated sample spot dominates the width. A Gaussian fit of the radially integrated experimental diffraction ring of graphite gave a width of 0.99 deg $\pm$0.11 deg, as shown in Fig. 7.

Fat is an amorphous material and has a broader peak. The resultant integration for experimental ring of fat yielded a width of 1.21 deg $\pm$0.11 deg as shown in Fig. 8. The natural width of the fat was taken as a fitting parameter and varied until a Gaussian fit of the radially integrated simulated diffraction ring matched the experimental width. This required a natural

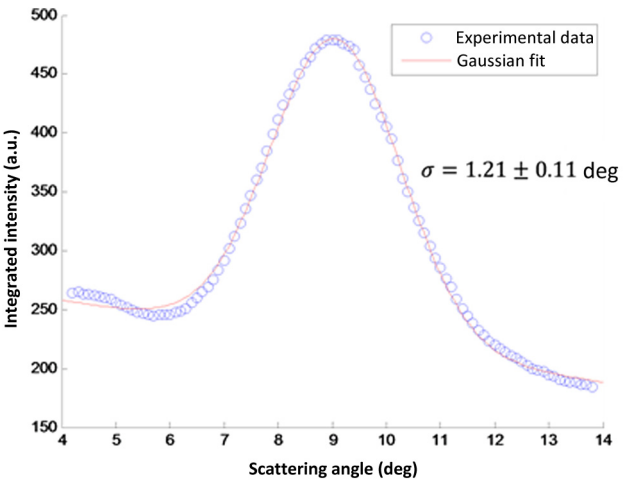

Fig. 8 The Gaussian fit of integrated intensity of the experimental fat ring, a linear fit was used for the fat background since the peak was asymmetric. The low angle intensity is high due to leakage around the beam stop which blocks the direct beam.

width of about 0.7 deg. The widths for cancer and fibroglandular tissue were taken from the literature.[4]

The areas under the Gaussian fit of the measured curves for fat and graphite were calculated to be 1030 ± 33 and 781 ± 20. By calculating the absolute diffracted intensity for graphite using Eq. (18) and the ratio between peak areas of fat and graphite, the absolute diffracted intensity of fat was determined and used in the simulation. The diffracted intensity for fibroglandular tissue was determined using ratios of fat to fibroglandular tissue coherent scatter coefficient ratio from the literature.[31] The diffracted intensity for cancer was determined using the fat to cancer peak area ratio from the literature.[32]

3.3 *Spectrum Simulation*

To simulate the real experiment, the actual spectrum was obtained at different voltages. Measurements were taken for three tube voltages, 30, 40, and 47.5 kV.[15] A linear search method using the CDF for the given discrete spectrum was used to simulate the given spectral distribution. The measured spectrum from the Oxford molybdenum source at a tube voltage of 47.5 kV is compared to the simulated spectrum in Fig. 9.

3.4 *Grid Transmission*

For a linear focused grid, the lead strips are tilted so that they all point at a common line at the focal distance away, as shown in Fig. 10. If the source of photons is at the focal distance, the grid transmission is

$$T_g = \frac{D}{W} T_{\text{interspace}}, \tag{20}$$

where D is the width of the interspace material, W is the repeat distance, and $T_{\text{interspace}}$ is the transmission of interspace material. If the photon source is not at the focus of the grid, the transmission of the grid is

$$T = T_g \frac{\mathrm{D}\ ?}{D}, \tag{21}$$

where D ? is the height above the exit point for a ray, as shown in Fig. 10.[16] The grid ratio

$$r = \frac{H}{D}, \tag{22}$$

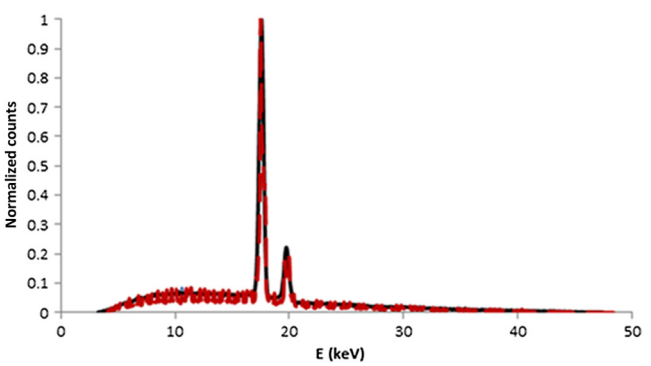

Fig. 9 Normalized lab measured spectrum[14] (black) and normalized simulated spectrum (red, dashed) of Mo source at 47.5 kV. The simulation and data coincide.

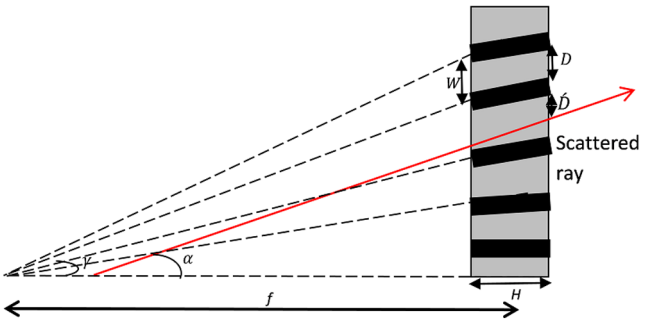

Fig. 10 Grid transmission depends on the point of impact.[16] The incident ray passes the grid when it hits the grid between lead strips if not absorbed by the interspace material.

determines the angular acceptance range for the grid. The transmission of the grid thus depends on the angle α between the horizontal and the incident ray, as shown in Fig. 10. For the simulation, α was calculated as

$$\alpha = \tan^{-1}\left(\frac{v_x}{v_z}\right), \tag{23}$$

where v_x/v_z is the ratio between the x component of velocity and the z component. The transmission depends on the difference between this angle and the angle γ of the lead strip at the point of impact, calculated as

$$\gamma = \tan^{-1}\left(\frac{x}{f}\right), \tag{24}$$

where x is the x component of the point of impact of the ray on the grid and f is the focal distance of the grid. If the difference between these two angles is larger than the acceptance angle, $\Delta\theta_g$, for the given grid ratio, r, the transmission is set to zero, otherwise it is transmitted with probability

$$T = T_g\left[1 - r\left(\frac{v_x}{v_z} - \frac{x}{f}\right)\right]. \tag{25}$$

This probability depends on the difference of angles. The angles here are small, so the arctangent was approximated as equal to the angle. T_g was taken from experimental data.[16] The normal incidence grid transmission was ~0.6 at 17.4 keV. A ratio of 10:1 gives an acceptance angle of $\Delta\theta_g = \tan^{-1}(1/r) = 5.7$ deg. The grid transmission is nearly zero for rays hitting at an angle greater than the acceptance angle on both sides from the central grid line, as shown in Fig. 11.

3.5 *Simulation Verification*

It was first necessary to verify the accuracy of simulation by comparison to the experimental results in a simple geometry. To model the experiment, graphite and fat were positioned adjacent to each other, graphite on top and fat at the bottom, as shown in Fig. 12. Graphite diffracts at 12 deg for the photon energy of 17.4 keV.[14,16,33] The experimental system compared the scatter from graphite and fat, to verify the simulation.

The simulated image signal-to-background ratio (SBR) between the two phantoms was calculated as

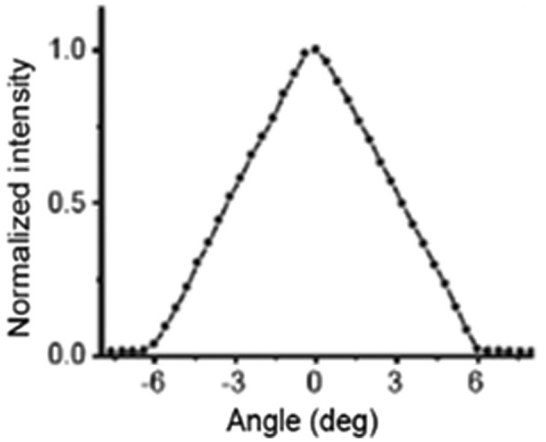

Fig. 11 Measured transmission of a collimated beam through the center of the grid as a function of grid tilt angle.[16]

$$\mathrm{SBR} = \frac{N_1 - N_2}{N_2}, \tag{26}$$

where N_1 and N_2 were the detected photon counts from the tissue of interest and the background, respectively. For the simulation of a buried carcinoma, the healthy breast tissue was considered as the background. To compute both intensities, a five-pixel wideband was selected, as shown in Fig. 13, and a vertical sum of photons at each horizontal position was calculated. The signal was taken as the maximum value of the profile in the selected band. For the simulations, the bands were taken at the known vertical location of the materials being compared. In a real experiment, the region would be selected based on a bright spot on the image, compared to a neighboring region, as is done for conventional radiography. The uncertainty was assumed to be Poisson noise calculated as the square root of the number of detected photons as in Eq. (10). The signal-to-noise ratio (SNR) was taken as

$$\mathrm{SNR} = \frac{N_1 - N_2}{\sigma_2}, \tag{27}$$

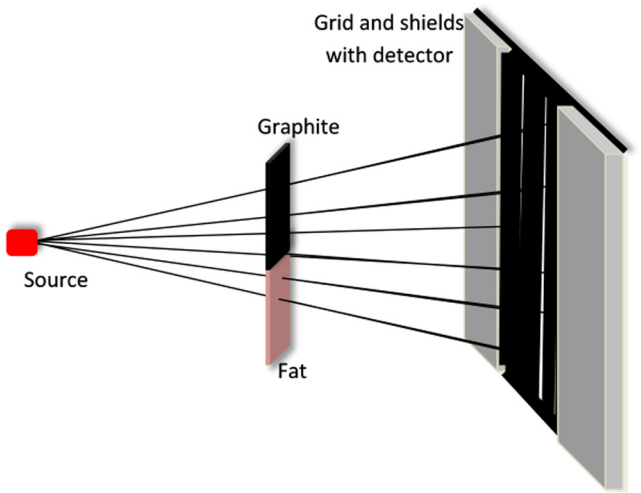

Fig. 12 Simulation setup. Graphite and fat were positioned adjacent to each other in order to model the experiment. The grid could be tilted at any angle with respect to the primary beam.

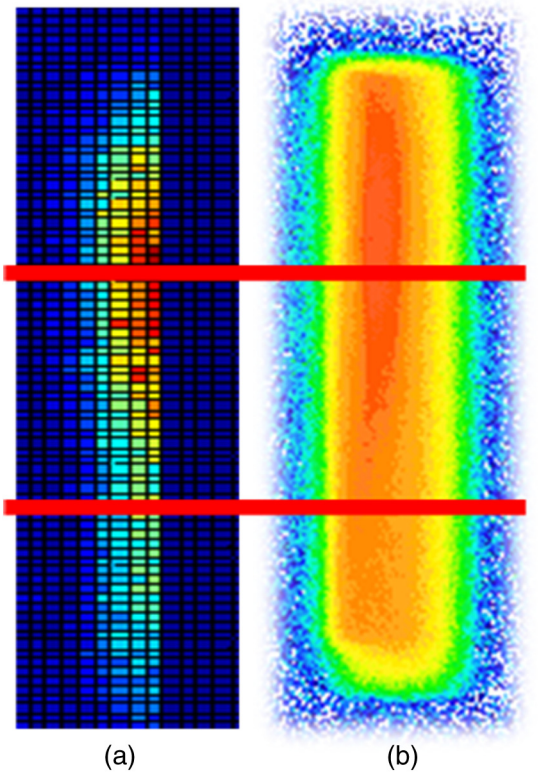

Fig. 13 (a) Simulated and (b) experimental images for the phantom in Fig. 12. The red bands denote where the intensity profiles have been drawn.

where $N_1 - N_2$ is the signal, defined as the difference between intensities from the two regions of interest on the image. The uncertainty in the SBR was taken as

$$\sigma_{\mathrm{SBR}} = \sqrt{\left(\frac{\partial \mathrm{SBR}}{\partial N_1}\right)^2 \sigma_1^2 + \left(\frac{\partial \mathrm{SBR}}{\partial N_2}\right)^2 \sigma_2^2}. \tag{28}$$

3.5.1 *Grid tilt angle*

For the first step of the simulation verification, the SBR values were computed for the sample in Fig. 12 for three different grid tilt angles. The simulated spectrum with a tube voltage of 47.5 kV was used to match the spectrum in the experiment. The grid had a 10:1 grid ratio. The comparison between experimental results[33] and simulation is shown in Fig. 14. The error bars for experimental results were large due to variability of the scatter from sample holders. Both experiment and simulation have the same trend, which shows that increased tilt angle improves the SBR.

3.5.2 *Voltage*

An SBR measurement was performed for the sample in Fig. 12 as a function of tube voltage. A 50-μm filter was used and shields were used instead of a grid to block the fat signal. The shield was located at 11 deg. The comparison between data[15] and simulation results is shown in Fig. 15. Both showed the trend of slightly improved SBR with increased voltage,

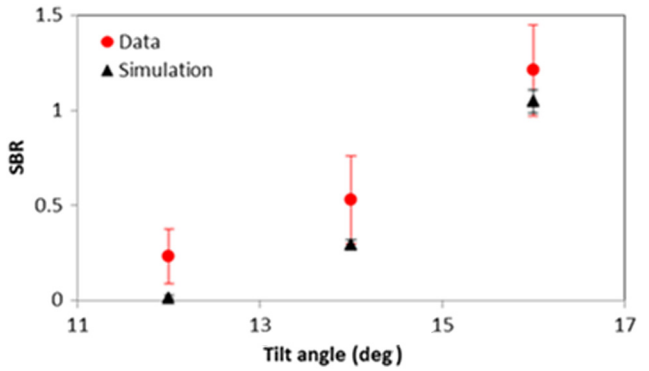

Fig. 14 A comparison between simulation and data[33] showing SBR versus grid tilt angle for the phantom of Fig. 12.

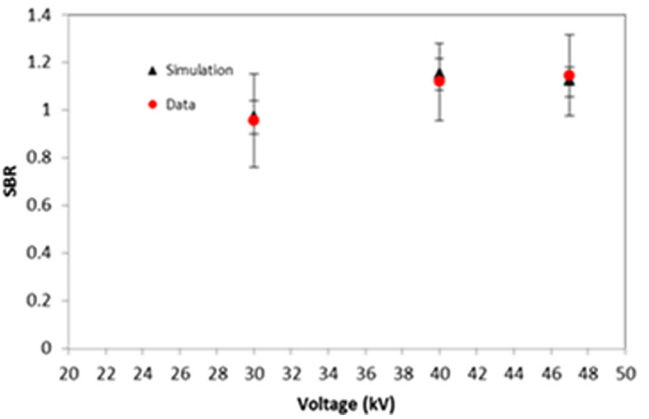

Fig. 15 A comparison between simulation and data[15] showing SBR versus voltage. Both showed the trend of improved SBR with increased voltage.

consistent with the relative increase in characteristic to bremsstrahlung ratio.

4 Results

4.1 *Parameter Optimization*

To find the optimal parameters which yield a maximum SBR and/or SNR, the code was run and tested for one parameter while keeping the other parameters unchanged. The sample for optimization was similar to the sample design of Fig. 12, but with carcinoma and a 50:50 mix of fat and fibroglandular tissue (instead of graphite and fat). Table 2 shows the fixed parameters.

4.1.1 *Grid*

Grid tilt angle. The results of varying the grid tilt angle are shown in Fig. 16. The optimal angle is 13 deg at which the SBR and SNR are maximized. Above that angle, the intensity decreases which yields poorer SBR and SNR. The results are different than in Fig. 14 because of the change in simulated phantom materials. In Fig. 14, fat and graphite, which have relatively large differences between the peak scatter angles, were used in order to compare with the experimental data. In Fig. 16, the comparison was between carcinoma and a 50:50 mix of fatty and fibroglandular tissues to optimize the system for a more realistic case.

Table 2 Fixed parameters used for the optimization.

Number of incident photons	1×10^7
Source-to-sample distance (mm)	400
Sample-to-detector distance (mm)	200
Spectrum	Measured x-ray spectrum at 47 kV with 138-μm Zr filter
Pixel size (mm)	2
Number of pixels in the intensity profile for contrast calculation	25 (5×5 pixels)

Grid ratio. Typical grid ratios used in mammography are 4:1 or 5:1. An analysis of the effect of increasing the grid ratio for a grid tilted at 13 deg was performed. Results are shown in Fig. 17. As the grid ratio increases, the SBR increases as long as the cancer signal is within the acceptance of the grid at the given tilt angle. For example, a 40:1 grid has an acceptance angle of 1.4 deg, so if tilted at 13 deg, it would block the healthy breast tissue background, ranging from 9 deg for fat to 11.8 deg for fibroglandular tissues. Here, the optimal ratio is 40:1, which yields the highest SBR and SNR for detection of the carcinoma peak at 13 deg. Higher ratios decrease the cancer signal, which yields poorer SBR and SNR.

4.1.2 *Shield location*

Figure 18 shows SBR and SNR as a function of low angle shield location without a grid. As the angle was increased, the shield blocked more of the breast background, which increases SBR until it starts to block the cancer signal at 13 deg. As a result, the optimal shield location is at 12.5 deg from the direct beam because it blocked much of the background tissue peak and yielded both high SBR and SNR.

4.2 *Breast Cancer Detection*

The median size at which breast cancer can be detected by conventional screening mammography is stated as ~7.5 mm.[34] To model the effectiveness of the system under realistic conditions, simulated sample dimensions were approximately the same as an average size breast. Breast sample dimensions used in the simulation were 40 mm for thickness, 60 mm for length, and 100 mm for width. However, the width for these static images is restricted by the slot width of 5 mm. Source-to-sample and sample-to-detector distances were 400 and 200 mm, respectively. Simulations were done first for tumors in a breast with a 100% fatty tissue. Figures 19(a) and 19(b) show the simulated coherent scatter images for 10- and 5-mm carcinoma inclusions, respectively. The tumors were modeled as cubes with linear dimensions of 10 or 5 mm. The shield was located at 12 deg from the primary beam to block the fat signal. As shown in Fig. 19, this technique is able to detect a 5-mm tumor. The SBR was 0.7 for the 10-mm tumor and 0.4 for the 5-mm tumor. These images were simulated using 100 million incident photons, or 3×10^4 photons/mm^2, which corresponds to

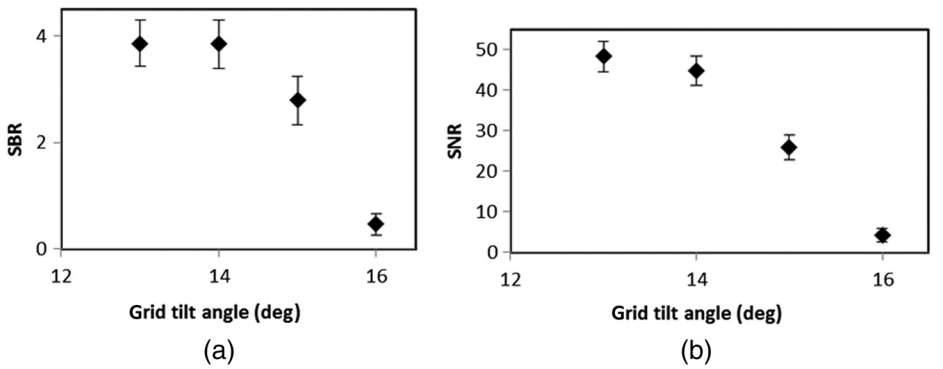

Fig. 16 (a) SBR and (b) SNR versus grid tilt angle. The optimal angle is 13 deg at which the SBR and SNR are maximized.

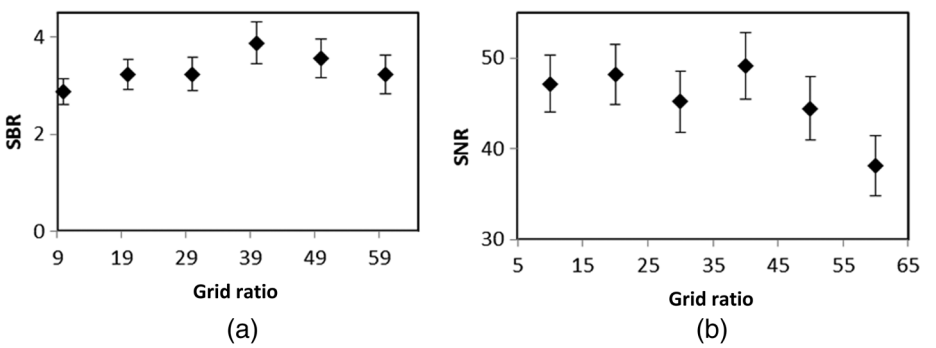

Fig. 17 (a) SBR and (b) SNR versus grid ratio. The optimal ratio is 40:1.

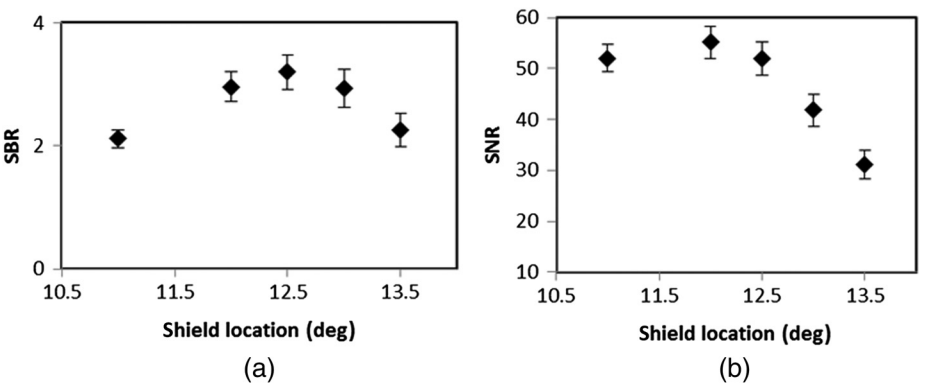

Fig. 18. (a) SBR and (b) SNR versus shield location.

approximately 2.5×10^{-3} mAs[35] compared to about 100 mAs, of the order of 2×10^{8} photons/mm^2 in clinical mammography.

To explore a more realistic case, the background tissue was changed to a 50:50 fatty/fibroglandular tissue mix. The shield was located at 13 deg from the primary beam to block the healthy breast tissue signal. Because of the low angular resolution of the system, it was expected that the system might have difficulty in this case. However, even a 5-mm tumor was still visible, as shown in Fig. 20. In this case, the background with no tumor, similar to that displayed in Fig. 19(c), was subtracted to highlight the tumor. The SNR value in this case was only 0.6, partly due to the low number of simulated photons. The SBR was 8%, substantially larger than the equivalent attenuation contrast of 1% for the same thickness of carcinoma in fibroglandular tissue. The cancer signals were clear visually in the model system even though it is not yet fully optimized for cancer detection.

The current study is limited by the simplicity of both the experimental phantom used to verify the results and the lack of background structure in the simulated phantom. Further experimental measurements are required to verify and further optimize the system, and to verify the results using simultaneous transmission mammography. However, because this technique does not require either high spatial or high angular resolution, it is expected that further refinement of the coherent scatter models will not substantially change the conclusion.

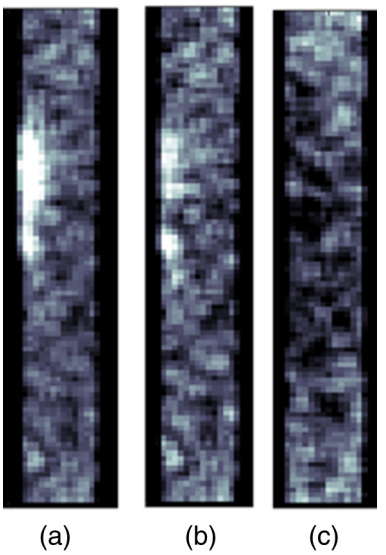

Fig. 19 Simulated cancer images for a (a) 10-mm and (b) 5-mm tumor in fatty tissue and (c) background image with no tumor. The cancer signal is still detectable for the smaller tumor.

Fig. 20 Simulated image for a 5-mm tumor in a 50:50 adipose/fibroglandular tissue after subtracting the no tumor background image [which was similar to that of Fig. 19(c)].

5 Conclusion

The modeling indicates that the technique has a potential as a simple addition to screening mammography. The model system can detect simulated carcinomas as small as 5 mm in diameter in a 50:50 adipose/fibroglandular tissue mixture. It is not yet fully optimized. Future study is indicated. In addition to refining the code to enhance the speed to allow larger numbers of photons, additional analysis is required to further optimize the system for carcinoma and to investigate the effect of breast density and breast thickness on detectability and SBR.

Acknowledgments

The authors are grateful for the support from the Department of Defense Breast Cancer Research Program Grant No. W81XWH-04-1-0752 and the National Institutes of Health No. 7 R01 EB0097.

References

1. J. Ferlay et al., *Cancer Incidence Mortality and Prevalence*, Worldwide IARC Cancer Base No. 5 version 2.0, IARC Press, Lyon (2004).
2. A. L. C. Conceição and M. E. Polettia, "Identification of molecular structures of normal and pathological human breast tissue using synchrotron radiation," in *6th Int. Conf. Medical Applications of Synchrotron Radiation*, Vol. **1266**, pp. 72–77, Melbourne, Australia (2010).
3. S. Sidhu et al., "Classification of breast tissue using a laboratory system for small-angle x-ray scattering (SAXS)," *Phys. Med. Biol.* **56**, 6779–6791 (2011).
4. S. H. Evans et al., "Measurement of small-angle photon scattering for some breast tissues and tissue substitute materials," *Phys. Med. Biol.* **36**, 7–18 (1991).
5. G. Kidane et al., "X-ray scatter signatures for normal and neoplastic breast tissues," *Phys. Med. Biol.* **44**, 1791–1802 (1999).
6. J. A. Griffiths et al., "Correlation of energy dispersive diffraction signatures and microCT of small breast tissue samples with pathological analysis," *Phys. Med. Biol.* **52**, 6151–6164 (2007).
7. E. J. Harris et al., "Evaluation of a novel low light level (L3 vision) CCD technology for application to diffraction enhanced breast imaging," *Nucl. Instrum. Methods Phys. Res. Sect. A* **513**, 27–31 (2003).
8. A. Taibi, G. J. Royle, and R. D. Speller, "A Monte Carlo simulation study to investigate the potential of diffraction enhanced breast imaging," *IEEE Trans. Nucl. Sci.* **47**, 1581–1586 (2000).
9. A. J. Kapadia et al., "Monte-Carlo simulations of a coded-aperture x-ray scatter imaging system for molecular imaging," *Proc. SPIE* **8668**, 86680B (2013).
10. W. M. Elshemey et al., "Monte Carlo simulation of x-ray scattering for quantitative characterization of breast cancer," *Phys. Med. Biol.* **54**, 3773–3784 (2009).
11. M. N. Lakshmanan et al., "An x-ray scatter system for material identification in cluttered objects: a Monte Carlo simulation study," *Nucl. Instrum. Methods Phys. Res. Sect. B* **335**, 31–38 (2014).
12. M. N. Lakshmanan et al., "Volumetric x-ray coherent scatter imaging of cancer in resected breast tissue: a Monte Carlo study using virtual anthropomorphic phantoms," *Phys. Med. Biol.* **60**, 6355–6370 (2015).
13. C. MacDonald, "Wide field coherent scatter imaging for radiography using a divergent beam," Patent, application 0794.075, (2009).
14. K. Kern et al., "A design for a coherent scatter imaging compatible with screening mammography," *J. Med. Imaging* (2016).
15. K. Kern et al., "Measurements and simulations of coherent scatter imaging as a simultaneous adjunct for screening mammography," *Proc. SPIE* **9412**, 941241 (2015).
16. W. Zhou and C. A. MacDonald, "Diffraction imaging with conventional sources," *Proc. SPIE* **7077**, 70770K (2008).
17. C.-J. Lai et al., "Comparison of slot scanning digital mammography system with full-field digital mammography system," *Med. Phys.* **35**(6), 2339–2346 (2008).
18. S. E. Bohndiek et al., "A CMOS active pixel sensor system for laboratory based x-ray diffraction studies of biological tissue," *Phys. Med. Biol.* **53**, 655–672 (2008).
19. M. Sanchez del Rio, "The very basics of SHADOW," 1998, Center for X-ray Lithography, http://www.esrf.eu/computing/scientific/raytracing/PDF/shadow_basics.pdf (2014).

20. X-5 Monte Carlo Team, "MCNP — a general Monte Carlo N-particle transport code, version 5," LA-UR-03-1987, Los Alamos National Laboratory (2003).
21. J. T. Bushberg, *The Essential Physics of Medical Imaging*, pp. 45–46, Lippincott Williams & Wilkins, Pennsylvania (2002).
22. C.T. Chantler et al., "X-ray form factors, attenuation, and scattering tables," National Institute of Standards and Technology, Parkville, Victoria, http://www.physics.nist.gov/PhysRefData/FFast/html/form.html (21 September 2009).
23. J. H. Hubbell and S. M. Seltzer, "Tables of X-ray mass attenuation coefficients and mass energy-absorption coefficients from 1 keV to 20 MeV for elements Z=1 to 92 and 48 additional substances of dosimetric interest," 1989, http://physics.nist.gov/PhysRefData/XrayMassCoef/tab1.html (2009).
24. ICRU, "Tissue substitutes in radiation dosimetry and measurement," Report 44 of the International Commission on Radiation Units and Measurements (Bethesda, Maryland) (1989), http://physics.nist.gov/PhysRefData/XrayMassCoef/tab2.html (2009)
25. M. Antoniassi et al., "Compton scattering spectrum as a source of information of normal and neoplastic breast tissues' composition," *Appl. Radiat. Isot.* **70**, 1451–1455 (2012).
26. J. H. Hubbell et al., "Inelastic scattering cross section in cm^2/g," *J. Phys. Chem. Ref. Data* **4**, 471–538 (1975). http://henke.lbl.gov/optical_constants/pert_form.html
27. H. Klug and L. Alexander, *X-Ray Diffraction Procedures for Polycrystalline and Amorphous Materials*, Wiley-Interscience Publication, New York (1974).
28. D. V. Rao et al., "X-ray scattering cross sections for molecules, plastics, tissues, and few biological materials," *J. Trace Microprobe Tech.* **20**, 327–361 (2002).
29. A. Guinier, *X-Ray Diffraction in Crystals, Imperfect Crystals, and Amorphous Bodies*, pp. 103–104, Dover Publications Inc., New York (1994).
30. A. P. Hammersley, ESRF, BP 220, 1997, Grenoble, France, http://www.esrf.eu/computing/scientific/FIT2D/ (2013).
31. M. E. Poletti et al., "X-ray scattering from human breast tissues and breast-equivalent materials," *Phys. Med. Biol.* **47**, 47–63 (2002).
32. W. M. Elshemey et al., "The diagnostic capability of x-ray scattering parameters for the characterization of breast cancer," *Med. Phys.* **37**(8), 4257 (2010).
33. L. Peerzada et al., "Potential for cone beam scatter imaging in screening mammography," *Proc. SPIE* **8313**, 831304 (2012).
34. J. Michaelson et al., "Estimates of the sizes at which breast cancers become detectable on mammographic and clinical grounds," *J. Women's Imaging* **5**(1), 3–10 (2003).
35. S. M. Lee and C. A. MacDonald et al., "X-ray tube sources," in *Handbook of Optics*, M. Bass, Ed., 3rd ed., Vol. **54**, pp. 54.3–54.7, McGraw-Hill Professional, New York (2001).

Laila Hassan emigrated from Yemen and received her doctorate from the University at Albany, SUNY, in 2015, where she is a researcher and an adjunct.

Carolyn A. MacDonald is a professor of physics at UAlbany. Her research is concerned with the development of x-ray technology for medical imaging and materials analysis. She is a frequent chair, program track chair, and participant in a number of SPIE conferences.